Published as S. C. Mangavelli, J. Yuan, and G. J. Brereton. J. Turbul., 22:434–460, 2021

Effects of surface roughness topography in transient channel flows

By Sai C. Mangavelli, Junlin Yuan† and Giles J. Brereton

Department of Mechanical Engineering, Michigan State University, East Lansing, MI, USA

The dynamical effects of roughness geometry on the response of a half-height turbulent channel flow to an impulse acceleration are investigated using direct numerical simulations. Two rough surfaces different in the surface height spectrum are compared between themselves and with a smooth-wall baseline case. Both rough cases develop from a transitionally rough state to a fully rough one. Results show that on rough walls the thickness of the roughness sublayer (RSL), defined as the layer with significant form-induced stresses, stays almost constant. The ensemble-average flows inside the RSL stays close to equilibrium throughout the transient. This is shown by the form-induced perturbations largely scaling with the mean velocity at the edge of the RSL. Inside the RSL, turbulence develops rapidly to the new steady state, accompanied by substantial changes in the Reynolds stress balance. In contrast, the flow above the RSL recovers long after the sublayer is fully developed, without a significant change in Reynolds stress balance. The geometry of the roughness plays an important role in determining the rate of response of turbulence throughout the boundary layer. This work provides detailed explanation of the suppression of reverse transition by surface roughness in response to a mean flow acceleration.

1. Introduction

In engineering applications, wall-bounded flows are frequently subjected to external effects such as freestream pressure gradients and unsteadiness, which have been studied extensively. Strong favorable free-stream pressure gradients (FPG) can attenuate turbulence and cause reverse transition to a quasi-laminar state, while adverse ones (APG) may result in flow separation: see, for examples, Jones & Launder (1972), Narasimha & Sreenivasan (1973), Bourassa & Thomas (2009), Piomelli & Yuan (2013), and Volino (2020) for discussions of favorable pressure gradients and Na & Moin (1998), Skote & Henningson (2002), Cheng *et al.* (2015), and Wu & Piomelli (2018) for adverse ones. Unsteady flows, and especially non-periodic transient ones, share some common features with spatially accelerating and decelerating flows, when viewed using the concept of the equivalent convection velocity (He & Jackson 2000). In this work, we focus on turbulence adjacent to rough walls when the flow undergoes abrupt acceleration.

Wall roughness plays important roles in multiple areas of fluid mechanics and many studies have been carried out to improve understanding of the dynamics of turbulent flows over rough walls, in both engineering and environmental applications. Readers are referred to Raupach *et al.* (1991), Jiménez (2004) and Chung *et al.* (2021) for reviews. Research efforts on the simultaneous effects of non-equilibrium acceleration and surface roughness have been the focus of several studies. Spatial flow acceleration over rough walls was investigated experimentally by Tachie *et al.* (2007) with rib roughness in an

† Email address for correspondence: junlin@msu.edu

open channel with converging side walls. They showed that the friction coefficient, the mean velocity defect, and the Reynolds shear stress were largely independent of the pressure gradient, possibly due to the limited streamwise distance over which the FPG was applied. Cal *et al.* (2009) performed experimental studies of roughness in quasi-equilibrium boundary layers with mild accelerations achieved using a tilted bottom wall. They found that the FPG increased the intensity of turbulent fluctuations adjacent to rough walls when compared to smooth ones, for which reverse transition was observed under the same pressure gradient.

A strongly accelerating flat-plate boundary layer over sandgrain roughness was analyzed using direct numerical simulations (DNS) by Piomelli & Yuan (2013) and Yuan & Piomelli (2015) to identify the coupling between effects of roughness and acceleration. Wall roughness had the effect of preventing reverse transition by deactivating the stabilizing effect of acceleration: form-induced perturbations of the time-averaged velocity ($\widetilde{u}_i$) promoted greater isotropy in the Reynolds stress through mechanisms that were not present in flow over a smooth wall. Specifically, an additional 'form-induced' production mechanism hereafter called P_s^f arises due to spatial gradients in $\widetilde{u}_i$. This term predominantly augments the production of wall-normal and spanwise Reynolds stresses, thereby contributing to more isotropic stresses over rough walls than over smooth ones. Enhanced pressure redistribution associated with form-induced velocities was also thought to modify the stress balance near the wall.

The response of turbulent channel flows to an impulse-like increase in flow rate, over smooth and rough walls, was characterized by He & Seddighi (2013) and Seddighi *et al.* (2015). In the case of a smooth wall, a three-stage process was identified. The initial phase was characterized by a decrease of friction coefficient and long streaky structures near the wall. As the flow recovered, turbulence spots were formed near the wall, which disturbed the stability of these long streaks and eventually merged and established a new steady state. In the presence of pyramid roughness, transition occurred earlier and without the reverse transition phase observed in the smooth-wall case. The transition was shown to be similar to roughness-induced laminar-to-turbulent transition, with the formation and breakdown of strong counter-rotating hairpin vortices near the roughness elements. These observations are similar to those made by Yuan & Piomelli (2015) for a spatially accelerating boundary layer over sandgrain roughness. Furthermore, for an oscillatory channel flow with rough walls (Ghodke & Apte 2016, 2017), additional production and transport of turbulent kinetic energy (TKE) due to form-induced perturbations was observed and this P_s^f was found to have a greater effect on the TKE budgets in an oscillatory channel flow than in a fully developed, steady, rough-wall channel flow.

In the studies described above, it was observed that in an accelerating turbulent boundary layer wall roughness acts to suppress the stabilization effect of acceleration. However, the connection between the geometry of surface roughness and this effect on turbulence is not well understood, particularly in developing, non-equilibrium flows. Furthermore, many practical roughness topographies include a multitude of roughness scales. For example, natural rough surfaces encountered in landscape topography and bathymetry are fractal-like (Passalacqua *et al.* 2006) in their geometry, with the longest wavelengths of roughness-height variation sometimes comparable to or larger than the boundary layer thickness (i.e. heterogeneous roughness). For this reason, we now summarize relevant research studies of multiscale surface roughness.

A major focus of the effects of multiscale roughness has been on surface-induced mean secondary flows (or streamwise rollers) when large-scale spanwise heterogeneities of

roughness geometry are present. Representative studies include Mejia-Alvarez & Christensen (2013), Vanderwel & Ganapathisubramani (2015), and Yang & Anderson (2018), among others. The hydrodynamic drag and modeling strategies for these flows were also studied; see, for examples, Passalacqua *et al.* (2006), Yuan & Piomelli (2014*a*) and Barros *et al.* (2018). Detailed effects of a multiscale roughness on turbulent wall-bounded flow were described by Yuan & Aghaei Jouybari (2018) for fully developed channel flow. The intensity and distribution of the $\widetilde{u}_i$ field were shown to depend strongly on the particular roughness topography. The form-induced stress is produced mainly by the work of pressure drag against the mean velocity. Such work is weakened for surfaces characterized by long horizontal roughness wavelengths, as the long wavelengths do not contribute to pressure drag (Barros *et al.* 2018). In addition, P_s^f was found to be less sensitive to the change of topography than were the pressure-work terms, despite the sensitivity of $\widetilde{u}_i$ to the roughness topography. It is thought to be because P_s^f depends on the spatial gradients of $\widetilde{u}_i$, rather than the $\widetilde{u}_i$ value itself. However, it is important to note that these multiscale roughness effects have been studied only in fully developed turbulent channels and boundary layers.

From this review, it appears that many aspects of turbulent flow in the vicinity of walls with different kinds of roughness have been explained from analyses of numerical simulation results. However, this understanding is generally limited to effects of roughness in steady-state, developed flows. The corresponding effects in time- and space-unsteady flows have received little attention. For these reasons, this study focuses on an important transient-flow phenomenon—the suppression of relaminarization by surface roughness—with emphasis on the role in suppression of different kinds of roughness. To this end, we study the problem of the response of wall-bounded turbulence to an abrupt increase in the bulk velocity of flow in a channel, using a configuration similar to that of He & Seddighi (2015). To better understand the role of roughness topography, a smooth wall and two very different surface roughness geometries are used.

2. Objectives

Direct numerical simulations were conducted in transient half-height channel flows, in which abrupt increases in mass flow rate were imposed on an initially steady-state flow. Unlike a spatially accelerating boundary layer, where the roughness wavelengths are constrained by the length scale of the mean velocity variation, a transient channel-flow simulation can accommodate roughness wavelengths as long as the channel itself, because of the use of a periodic streamwise boundary condition. The behavior of turbulent flow over two surfaces with different roughnesses was compared to that in the baseline case of smooth-wall flow. In this paper, Sec. 3 introduces the governing equations and details of the numerical solution, roughness geometries, and simulation parameters. Section 4 compares the results of the smooth-wall and the two rough-wall cases for both the initial steady state (before the transient started, Sec. 4.1) and the recovery after the transient was imposed. Transient flow comparisons were carried out for the mean velocity (Sec. 4.2), form-induced velocities (Sec. 4.3), the Reynolds stresses (Sec. 4.4), and the Reynolds stress budgets (Sec. 4.5).

3. Methodology

3.1. *Governing equations*

The incompressible flow of a Newtonian fluid is governed by the equations of conservation of mass and momentum:

$$\frac{\partial u_i}{\partial x_i} = 0, \tag{3.1}$$

$$\frac{\partial u_j}{\partial t} + \frac{\partial u_i u_j}{\partial x_i} = -\frac{\partial P}{\partial x_j} + \nu \nabla^2 u_j + F_j, \tag{3.2}$$

where: x_1, x_2 and x_3 (or x, y and z) are, respectively, the streamwise, wall-normal and spanwise directions, and u_j (or u, v and w) are the velocity components in those directions; $P = p/\rho$ is the modified pressure, ρ the density and ν the kinematic viscosity. The term F_j in Equation (3.2) is a body force of the immersed boundary method (IBM) used to impose non-slip/penetration boundary conditions at the rough surface, which is well-resolved by the grid. The method is based on the volume-of-fluid approach (Scotti 2006); its detailed implementation in the in-house fluid solver and validation are described in Yuan & Piomelli (2014*c*) and Yuan & Piomelli (2014*b*). Specifically, the volume fraction occupied by the fluid $\phi(x, y, z)$ in each grid cell is calculated during pre-processing. It is used to calculate the force $F_1(x, y, z, t)$ at each time step, to decrease the momentum in each grid cell by a fraction of $(1 - \phi)$. The F_1 values are non-negligible in the boundary cells of roughness, and are negligible elsewhere. The simulations were performed using a well-validated code that solved the governing equations (3.1) and (3.2) on a staggered grid using second-order central differences for all terms, second-order accurate Adams-Bashforth semi-implicit time advancement, and MPI parallelization (Keating *et al.* 2004).

In the roughness sublayer, the presence of roughness elements leads to spatial heterogeneity in ensemble-averaged variables. Such heterogeneity was separated from turbulent fluctuations using a double-averaging (DA) decomposition (Raupach & Shaw 1982),

$$\theta(x, y, z, t) = \langle \overline{\theta} \rangle(y, t) + \widetilde{\theta}(x, y, z, t) + \theta'(x, y, z, t), \tag{3.3}$$

where θ is some local, instantaneous flow variable, $\langle \theta \rangle$ is the intrinsic spatial average in the (x, z)-plane, $\langle \theta \rangle(y, t) = 1/A_f \int_{A_f} \theta dA$ (where A_f is the area occupied by fluid at elevation y), $\overline{\theta}$ denotes the ensemble average (the 'mean' component), $\theta' = \theta - \overline{\theta}$ is the turbulent fluctuation from $\overline{\theta}$, and $\widetilde{\theta} = \overline{\theta} - \langle \overline{\theta} \rangle$ is the dispersive (or form-induced) fluctuation. A superficial spatial averaging is also used; it is defined as $\langle \overline{\theta} \rangle_s(y, t) = 1/A_f \int_{A_o} \theta dA$, where $A_o = L_x L_z$ is the total horizontal area of the simulation domain and L_{x_i} is the domain size in x_i.

The streamwise component of the IBM body force, $F_1(x, y, z, t)$, can be integrated in the wall-normal direction to yield the total hydrodynamic drag at a (x, z) location and a time t, including both viscous and pressure drags. The wall shear stress τ_w is then calculated as the ensemble-averaged total drag per domain horizontal area:

$$\tau_w(t) = \frac{\rho}{L_x L_z} \int_{\mathcal{V}} \overline{F}_1(x, y, z, t) \, \mathrm{d}x \, \mathrm{d}y \, \mathrm{d}z, \tag{3.4}$$

where $\mathcal{V}$ represents the volume of the simulation domain. The friction velocity is then obtained as $u_\tau(t) = \sqrt{\tau_w/\rho}$. This method of τ_w calculation was validated by Yuan & Piomelli (2014*c*) in a fully developed channel flow over sandgrain roughness by comparing with the total drag calculated from the mean momentum balance.

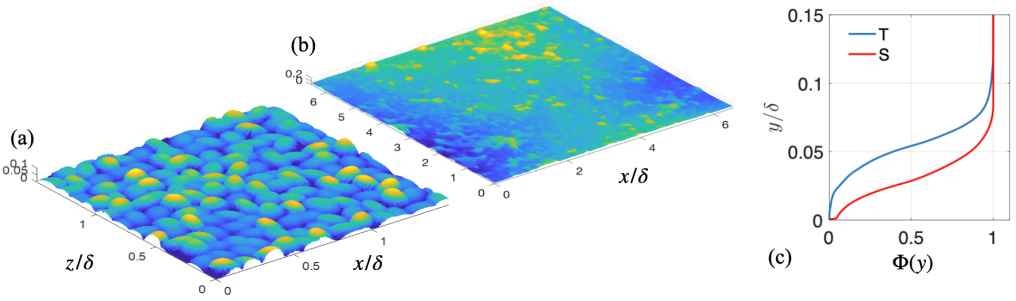

FIGURE 1. A fraction of sandgrain (a, case S) and turbine-blade (b, case T) rough surfaces colored by height. (c) Variation of roughness geometry functions along y.

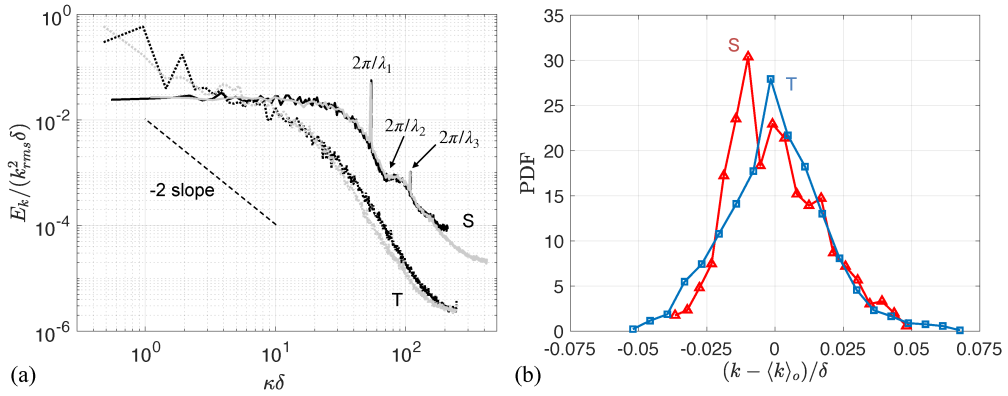

FIGURE 2. (a) Power spectrum of surface height fluctuations in cases S (———) and T (- - -) with wavenumbers κ in x (black) and z (grey). For S, λ_1, λ_2 and λ_3 are the three semiaxes of an ellipsoid grain (Scotti 2006). (b) PDFs of surface height fluctuations for cases S and T; normalization is done such that area below curve is one.

3.2. *Rough surfaces*

Two quite different surfaces roughnesses were considered: one synthetic sandgrain roughness 'S' (Fig. 1a), and one replicated from a surface scan on a hydraulic turbine blade 'T' (Fig. 1b). Flow over these two surfaces was studied in fully-developed half-height channels by Yuan & Aghaei Jouybari (2018), who compared details of their surface-geometric parameters. Figure 1(c) compares the roughness geometry functions between the two roughnesses. It increases with y and reaches its maximum value of 1 at $y = k_c$. The power spectrum and the probability density functions (PDFs) of local surface height fluctuations $k(x,z) - \langle k(x,z)\rangle_o$ are compared in Fig. 2. Here, operator $\langle\cdot\rangle_o$ denotes averaging across the wall-parallel plane. The 'sandgrain roughness' surface S was created as a uniform distribution of randomly oriented ellipsoids of the same geometry (Scotti 2006). Its roughness height distribution was characterized by dominant wavelengths much smaller than the channel half-height δ; the spectral decay occurs only for scales smaller than the grain size. In contrast, surface T yields an approximate power-law decay of the power spectrum with a slope of -2, indicating similarity to a fractal geometry. The initial turbine roughness scan was mirrored in both x and z to produce the final T surface that satisfied periodic boundary conditions in x and z. When these roughness height distributions are compared with δ, surface S may be considered a homogeneous roughness,

Surface	R_a/δ	k_c/δ	k_{rms}/R_a	s_k	k_u	ES_x	ES_z	$(L_x, L_z)/\delta$
SM	0	0	0	0	0	0	0	(12, 6)
S	0.014	0.09	1.05	0.48	2.97	0.43	0.44	(12, 6)
T	0.014	0.13	1.17	0.20	3.49	0.10	0.08	(12, 12)

TABLE 1. Geometrical parameters of the sandgrain (S), turbine roughness (T) and the smooth wall (SM). δ is channel half height; Ra is first-order moment of height fluctuations; k_c is maximum peak-to-trough height (crest height); k_{rms}, s_k and k_u are the root-mean-square, skewness and kurtosis of height fluctuations; ES_{x_i} is the effective slope in x_i; L_{x_i} is the domain size in x_i.

Surface	Re_{b0}	$Re_{\tau 0}$	Ra/δ	k_c/δ	$k^+_{s,\infty}$	$(\Delta x^+, \Delta y^+_{\mathrm{min}}, \Delta z^+)$
SM	4,000	244	0	0	0	(4.0, 0.9, 2.0)
S	4,000	320	0.019	0.08	21	(5.0, 1.2, 2.5)
T	4,000	294	0.019	0.12	10	(3.4, 1.1, 3.4)

TABLE 2. Simulation parameters in the initial steady state (denoted by subscript '0'). Superscribe '+' indicates normalization by wall units (u_τ and viscous length scale $\delta_\nu = \nu/u_\tau$).

Surface	Re_{b1}	$Re_{\tau 1}$	Ra/δ	k_c/δ	$k^+_{s,\infty}$	$(\Delta x^+, \Delta y^+_{\mathrm{min}}, \Delta z^+)$
SM	12,000	626	0	0	0	(9.8, 2.3, 4.8)
S	12,000	1023	0.019	0.08	76	(15.3, 3.7, 7.6)
T	12,000	858	0.019	0.12	23	(10.1, 3.3, 10.1)

TABLE 3. Simulation parameters in the final steady state (denoted by subscript '1').

whereas surface T is heterogeneous (with important features at scales larger than δ). The PDFs of height fluctuations show that both roughness geometries are characterized by rather evenly distributed height values with respect to the average height. Case S shows slight bias toward lower height values.

Geometrical parameters of the two surface roughnesses are compared in Table. 1. Both surfaces share the same first-order moment of height statistics (R_a), and have very similar (with 10% difference) RMS roughness heights (k_{rms}), but quite different values of maximum peak-to-trough height (k_c, also called crest height), skewness (s_k) and effective slope (ES) in x or z. $k_c/\delta \leq 0.13$ for both cases. A smooth-wall baseline case 'SM' is used for purposes of comparison.

3.3. *Simulation Parameters*

Simulation parameters for all cases are listed in Tables 2 and 3. The initial and final steady states are denoted using subscripts '0' and '1', respectively. Parameters such as the Reynolds numbers and roughness crest heights were chosen to ensure that the transient and the final states of each flow corresponded to the Reynolds-number-independent fully rough regime of flow for both rough surfaces. The final steady state is reached at different times for different flow statistics; after the steady state is reached, the value of a flow quantity does not vary in time any more. Note that during the transient some quantities cross the final steady-state values before the steady state is reached; these

quantities include the frictional coefficient, dispersive stresses, and streamwise Reynolds stress, among others.

Here, $k_{s,\infty}$ is the corresponding equivalent Nikuradse sandgrain height in the fully rough regime, defined by Jiménez (2004). The values of $k^+_{s,\infty}$ in Tables 2 and 3 for both surfaces are deduced from the ratio $k_{s,\infty}/k_c$ determined in the study of Yuan & Piomelli (2014*a*), where a Reynolds number sweep was performed for each surface to identify the critical roughness Reynolds number $k^+_{s,cri}$ corresponding to the lower limit of the fully rough regime. In the final steady state, the values of $k^+_{s,\infty}$ are 76 and 23, for S and T respectively, while the respective values of $k^+_{s,cri}$ were found to be 60 and 20 (Yuan & Piomelli 2014*a*)—lower than the steady-state values of $k^+_{s,\infty}$—indicating that fully-rough flow had been achieved. Considering that both rough surfaces share the same value of Ra and slightly different Re_τ, the observation that case S yields a much higher value of $k^+_{s,\infty}$ indicates that it generates significantly more hydrodynamic drag than case T.

The domain sizes in x and z are $(12\delta, 6\delta)$ for cases SM and S, and $(12\delta, 12\delta)$ for case T. For case T, a larger spanwise domain is required to accommodate larger spanwise roughness wavelengths. For all cases, L_x were chosen similar to that used by He & Seddighi (2013) for a similar smooth-wall transient flow setup. In the study by He & Seddighi (2013), a similar u_{b1}/u_{b0} ratio of 2.6 was used, but the Reynolds numbers was much lower ($Re_b = 2825$ compared to 7404 herein). They found that $L_x/\delta \approx 12$ was sufficient for accommodating large-scale motions according to the two-point velocity correlations. For the rough cases, the near-wall u'_i coherence lengths are expected to be shorter than on a smooth wall. It is validated for cases S and T that the two-point correlation of u' at streamwise separation of a half of the domain size falls below 0.1 at $y/\delta = 0.3$ for all t^*.

The numbers of grid points are $(768, 273, 768)$, $(768, 263, 768)$ and $(1024, 259, 1024)$ in (x, y, z) for cases SM, S and T, respectively. The mesh is uniform in x and z while refined near the wall in y. At the final steady state (the more critical one for spatial resolution between the two steady states), $\Delta y_{\min} < 0.3$ for SM and Δy^+ falls between 0.6 and 1.7 in the layer below roughness crest for the rough cases. The stretching ratio of the non-uniform y grid is kept below 0.03. The grid sizes normalized by the local Kolmogorov lengthscale $\eta(y,t)$ are, for SM, S, and T cases respectively, 3-7, 4-9, 2-6 in x and 1-2, 2-4, 2-6 in z, throughout the transient. $\Delta y/\eta$ values are much smaller than those in x and z. For a curved channel flow, scales smaller than 15η were found to contribute to most of the dissipation (Moser & Moin 1987). Therefore the spatial resolution herein was believed to be sufficient to resolve the dissipative scales of turbulent motions. This is also supported by the small residuals found in Reynolds stress balances as discussed later in Sec. 4.5.

Aside from the requirement to resolve the small-scale motions, a rough-wall simulation also requires resolution of the roughness geometry. For the sandgrain roughness, the spatial resolution of the grain geometry was 8 and 16 points per grain in x and z, which was slightly higher than the resolution used by Yuan & Piomelli (2014*c*) (case R1 therein). For the turbine blade roughness, there is no single surface length scale and so an equivalent 'roughness element' size is defined based on the Taylor microscale of surface height fluctuations λ as in Yuan & Piomelli (2014*a*). λ was resolved by 10 points in both x and z, same as in Yuan & Aghaei Jouybari (2018). For the rough-wall cases, $y = 0$ was chosen at the lowest trough elevation of the surface. The virtual origin, d—defined as the centroid of the y-profile of averaged drag distribution (Jackson 1981)—was used to offset the wall-normal profiles when comparing results between different cases.

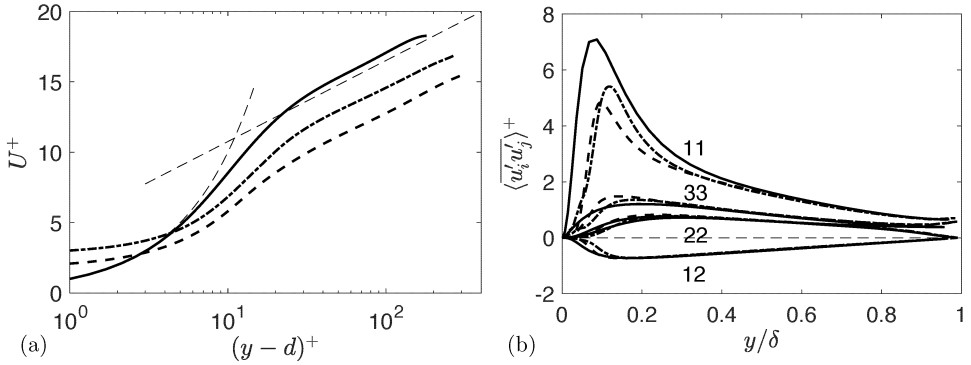

FIGURE 3. (a) DA streamwise velocity, (b) Reynolds stress components at $t^* = 0$, for SM (———), S (– – –) and T (– – –) cases. $d = 0$ for SM. In (a), thin dashed lines are $U^+ = (y-d)^+$ and $U^+ = 1/0.4 \log(y-d)^+ + 5.0$.

The flow configurations used were similar to those of He & Seddighi (2013). A strong temporal acceleration was achieved by imposing a temporally varying streamwise pressure gradient, which was adjusted at each time step to produce a prescribed ramp-like linear increase in the mass flux from u_{b0} to u_{b1} (where u_b is the instantaneous bulk velocity). At time $t^* \equiv tu_{b0}/\delta = 0$, the mass-flow rate was subjected to a ramp increase (during a short time interval $\Delta tu_{\tau 0}/\delta = 0.08$) to achieve $Re_{b1} = 3Re_{b0}$. The flow was then allowed to develop until a new equilibrium state was reached. This ramp-like acceleration was strong enough to cause departure from equilibrium above a smooth wall. A half-height channel was simulated, with symmetric boundary conditions applied at the top boundary, to reduce the computational cost as compared to a full channel. Periodic boundary conditions were applied in x and z.

For each case, the transient simulations were repeated with different initial conditions (obtained from a separate fully developed half-height channel simulation at $Re_{\tau 0}$ for each case). The transient simulation was repeated 20 times for SM and S and 40 times for T. The flow statistics at each t^* were calculated from ensemble averaging. The adequacy of the number of ensembles from which averages were constructed was tested by halving it, which led to changes of around 0.5% in the mean streamwise velocity and less than 4.5% in the Reynolds stresses.

4. Results

4.1. *Initial steady state flows*

At $t^* = 0$, the wall-normal profile of the DA streamwise velocity $U \equiv \langle \overline{u} \rangle$ in wall units is shown in Fig. 3(a) for all cases. The smooth-wall profile compares well with the classical law-of-the-wall, except that the logarithmic intercept B is measured as 5.5 (assuming the von Kármán constant is 0.4), within the range of values that are typically observed (within 5% of 5.2 according to Pope (2000)). Nagib & Chauhan (2008) fitted parameters for the logarithmic law based on available data in the literature and observed that B falls between 5 and 6 for channel flows at displacement thickness Reynolds numbers (Re_{δ^*}) between 300 and 2,000; the present smooth-wall case (SM) gives a Re_{δ^*} of 715, which falls in this range. Compared to case SM, the presence of roughness yields a velocity deficit (ΔU^+) in the logarithmic region as expected. Case S gives a higher ΔU^+, consistent

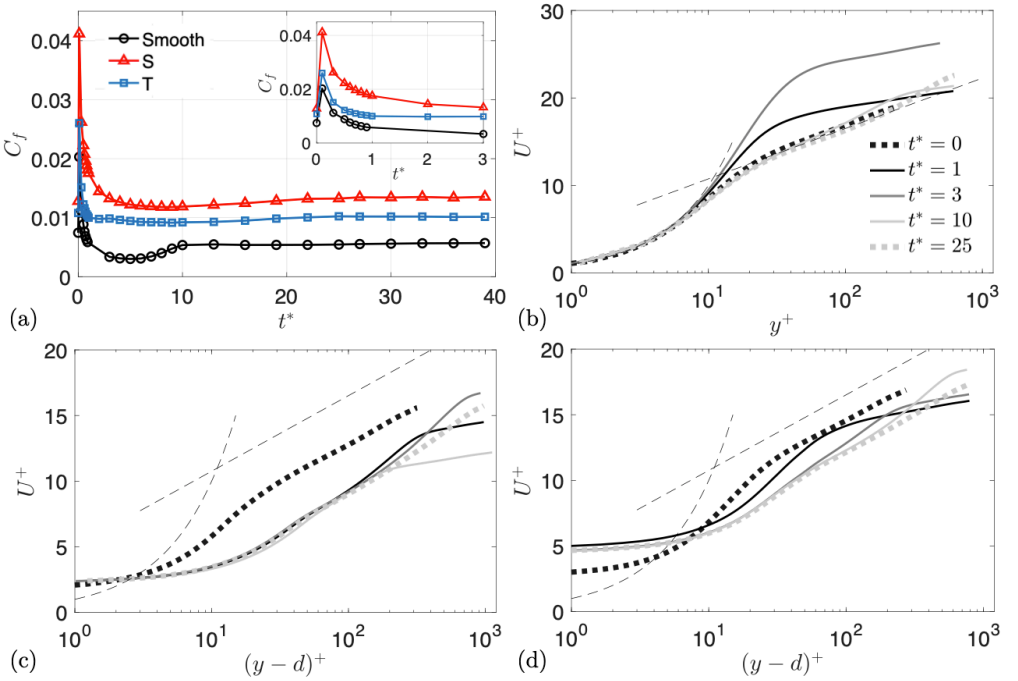

FIGURE 4. (a) Temporal variation of C_f for all cases; inset magnifies the plot at small t^* values. Streamwise DA velocity normalized by instantaneous wall units in (b) smooth case and cases with surface S (c) and surface T (d). - - - : $U^+ = (y-d)^+$ and $U^+ = 1/0.4\log(y-d)^+ + 5.0$.

with the knowledge that surface S leads to higher drag generation than surface T (Yuan & Aghaei Jouybari 2018).

Figure 3(b) compares all non-zero components of the Reynolds stress tensor among all cases. The outer-layer similarity is demonstrated for all tensor components. The near-wall layer (where no matching is observed between rough and smooth cases) corresponds to the RSL, defined herein as the near-wall region where the dispersive perturbations are significant with respect to the local mean momentum (see Sec. 4.3). In the RSL, similar observations are made as those by Yuan & Aghaei Jouybari (2018) for the same rough surfaces at a higher Reynolds number of $Re_\tau = 1000$, including a stronger 11 component and weaker 22 and 33 components of the Reynolds stress tensor in Case T compared to S.

The Reynolds stresses at the channel centerline depart slightly from those at the centerline in a full channel simulation. This is due to the symmetric boundary condition at the top boundary used herein to simulate a half-height channel. Specifically, here v' is imposed to be zero at $y/\delta = 1$. The turbulence kinetic energy is redistributed to u' and w', which is probably the reason for the slightly elevated 11 and 33 Reynolds stress components at $y/\delta = 1$. Similar phenomena were observed by Scotti (2006).

4.2. *Temporal variation of ensemble-averaged velocities*

First, the friction coefficient is obtained by normalizing the instantaneous τ_w with the initial bulk velocity,

$$C_f(t) = \frac{\tau_w(t)}{\rho u_{b0}^2/2}, \tag{4.1}$$

and plotted in Fig. 4(a). In all cases C_f undergoes a sudden increase immediately after $t^* = 0$ in response to the impulse increase of u_b. Following this jump, C_f decreases rapidly as the flow starts to recover. In the smooth-wall case the $C_f(t)$ curve shows a dip (lower than the long-time value) with a minimum C_f found at around $t^* = 5$. For this flow in the corresponding t^* range, He & Seddighi (2013) observed elongated low-speed streaks, laminar-like mean velocity profiles (also shown in Fig. 4b), more anisotropic Reynolds stress tensor (also shown later in Fig. 9), and increased TKE production with a frozen pressure strain term (also shown later in Fig. 12). These phenomena are indicative of a reverse transition process toward a quasi-laminar state discussed for spatially developing turbulence under a strong freestream acceleration (see e.g. Narasimha & Sreenivasan (1973) and Piomelli & Yuan (2013)). The new steady state is reached at $t^* \approx 10$ for the smooth case. In the presence of roughness, there is no appreciable dip in C_f regardless of roughness geometry, indicating that the flows do not undergo reverse transition. Absence of quasi-laminarization on a rough-walled boundary layer subjected to strong streamwise acceleration was also reported by Yuan & Piomelli (2015). Also notice that C_f is lower for case T compared to case S throughout the transient.

The DA streamwise velocity profiles U against y (offset by the virtual origin d), both normalized by instantaneous wall units, are plotted in Fig. 4(b-d). The value of d stays almost invariant in time for both rough cases throughout the transient: $d/\delta \approx 0.045$ and 0.058 for cases S and T, respectively. On the smooth wall, U^+ departs significantly from the logarithmic law-of-the-wall during reverse transition ($t^* < 5$). Initially, the U profile is characterized by a thickened viscous sublayer and an increase of the von Kármán constant κ, as shown at $t^* = 1$. At $t^* = 3$, the profile becomes laminar-like, indicating that the flow is in the quasi-laminar state. The logarithmic profile is recovered after the re-transition. For both rough cases, κ also increases temporarily. For case T, this is shown at $t^* = 1$, while for case S, this happens between $t^* = 0$ and 1 and is not shown in the figure. On T roughness, the increase of κ is shown at $t^* = 1$. A higher κ was also observed for spatially developing boundary layer on the sandgrain roughness (Yuan & Piomelli 2015). Such phenomenon and the difference between cases S and T are explained in Sec. 4.4. Lastly, we observed that the logarithmic region recovers faster in case S than in case T. These observations on κ in cases S and T will be explained in Sec. 4.4.

The U profiles with linear y axis are compared in Fig. 5 in the near-wall region. For all cases, immediately after the impulse acceleration the near-wall rate of shear $(\partial U/\partial y)$ increases rapidly to values similar to the final steady state. Nikora *et al.* (2004) showed that a constant roughness geometry function, $\Phi(y) \equiv A_f(y)/A_o$ leads to an exponential U profile up to the crest height, while a monotonically increasing $\Phi(y)$ as the crest is approached—as in the present cases—lead to a linear velocity profile. Quasi-linear U profiles below k_c are indeed observed for both cases S and T throughout the transient. Notice that for case T the sampling of large surface wavelengths is not as sufficient as the small wavelengths in case S, leading to slight undulation of the quasi-linear $U(y)$ profile below k_c for case T.

In a developing flow, the hydrodynamic drag is more directly connected to the near-wall velocity than to the bulk velocity (Yuan & Piomelli 2015). A measure of the near-wall

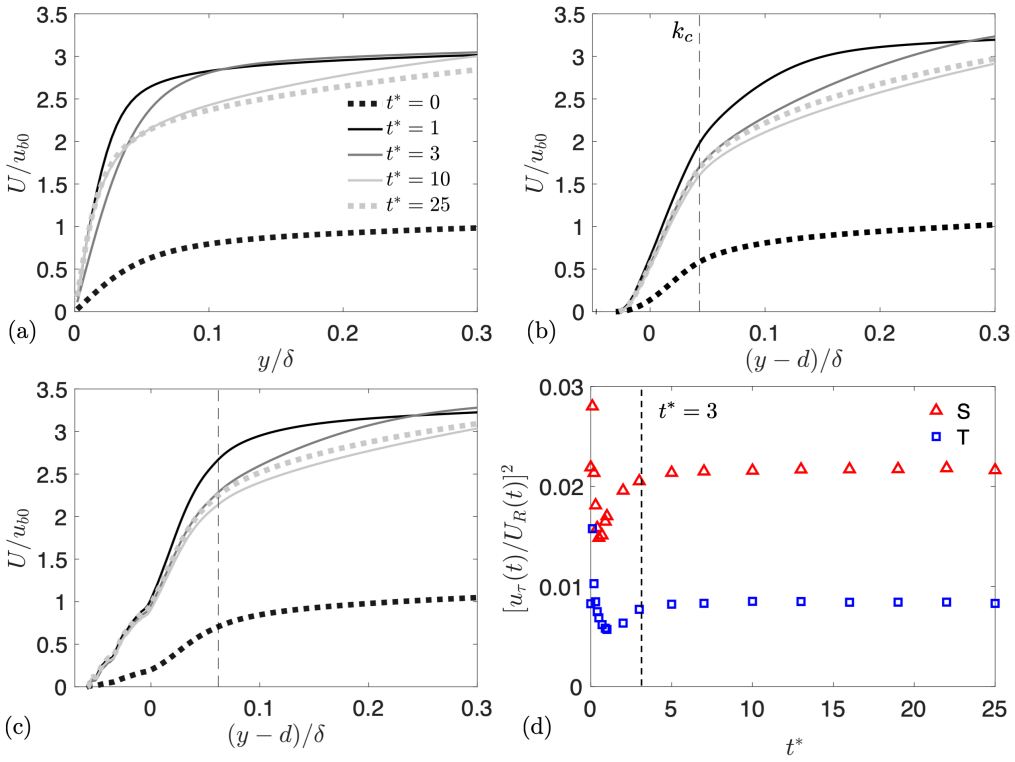

FIGURE 5. (a-c) U profiles against y in linear scaling, for cases SM (a), S (b) and T (c). (d) Instantaneous u_τ normalized by the instantaneous value of the velocity scale at the edge of the roughness sublayer, U_R.

velocity scale is the velocity at the edge of the RSL, $U_R(t) \equiv U(y_R, t)$, where y_R is the thickness of the RSL, to be further discussed in Sec. 4.3. The RSL is defined herein for all t^* as the near-wall region where $\langle \widetilde{u}^2 \rangle^{1/2}/U < 0.1$, similar to the approach used by Pokrajac *et al.* (2007) (except for a different threshold value used). Throughout the course of the transient, y_R/k_c takes values (1.10 ± 0.13) and (1.05 ± 0.10) for cases S and T, respectively. In other words, the RSL thickness varies weakly in time.

Figure 5(d) shows the ratio $[u_\tau(t)/U_R(t)]^2$ for the two rough cases. After $t^* \approx 3$, both cases give a constant ratio, indicating that the near-wall flows are fully developed even though the U profile shape farther from the wall still varies in time as shown in Fig. 5(b-c). For $t^* < 3$, the variation of $u_\tau(t)/U_R(t)$—including the initial spike at $t^* = 0$ and the later dip—shows the non-equilibrium response of the near-wall $\overline{u}(\boldsymbol{x}, t)$. The minimum $u_\tau(t)/U_R(t)$ occurs at $t^* \approx 0.5$ and 1.0 for cases S and T, respectively. These time instances are much later than the mean mass flow rate ramp up which ends at $t^* = 0.08$. The observation that the minimum $u_\tau(t)/U_R(t)$ is reached at an earlier t^* in case S than in case T is consistent with the earlier recovery of Reynolds stresses inside the RSL discussed in Sec. 4.4. The ratio $u_\tau(t)/U_R(t)$ depends on individual variations of u_τ and U_R in time. The $C_f(t)$ variation (Fig. 4(a)) describes the variation of u_τ magnitude (as U_∞ is constant for $t > 0$). The $C_f(t)$ comparison shows that u_τ recovers more slowly on S than on T. Yet, the U_R variation is faster on S than on T, contributing to earlier recovery of RSL turbulence on S.

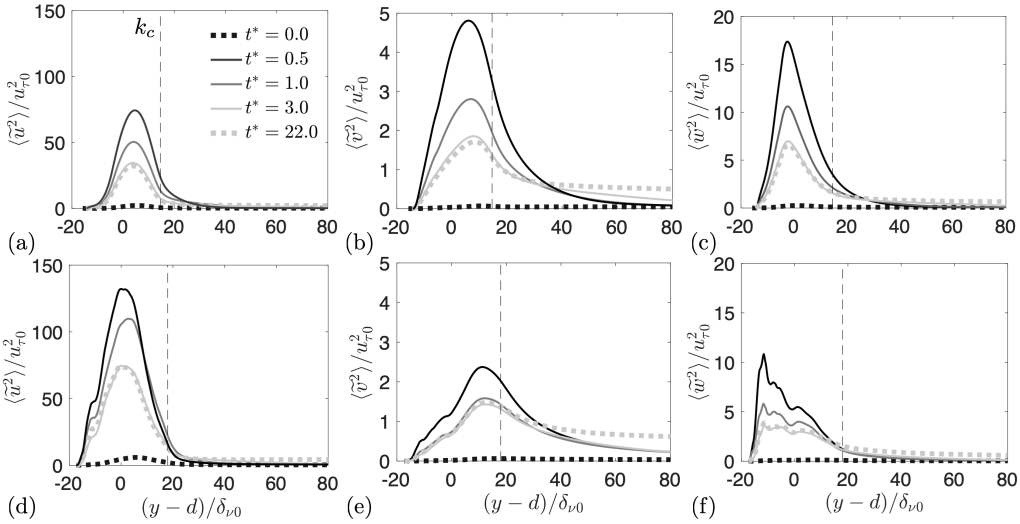

FIGURE 6. Wall-normal profiles of normal components of the dispersive stress tensor (normalized by $u_{\tau 0}^2$) for (a-c) case S and (d-f) case T.

4.3. *Temporal variations of dispersive stresses*

Figure 6 compares normal dispersive stresses for cases S and T at different times. In both cases, significant magnitudes of normal dispersive stresses are confined in a near-wall layer. All components increase immediately after the impulse acceleration, rapidly reaching the maximum values before $t^* = 0.5$. These maximum values are considerably higher than the values in the final steady state. After $t^* = 0.5$, all components rapidly decrease, reaching the steady-state values at $t^* = 3$. Notice that the stress profile shapes do not change significantly during the transient; the peak elevations vary only weakly. Figure 6 also shows that the RSL thickness, y_R, is not significantly affected during the transient.

Figure 5(a) show that the peak values of $\langle\widetilde{u}^2\rangle$ slight increases at large times ($t^* > 10$) for both cases. This is probably connected to the development of large scale secondary motions (high and low momentum regions) induced by spanwise roughness heterogeneity (Mejia-Alvarez & Christensen 2013; Vanderwel & Ganapathisubramani 2015), toward a higher-Reynolds-number new equilibrium state. Our earlier DNS study (Yuan & Brereton 2019) of open channel flows at a Re_τ of 1000 showed that the present roughness geometries with similar k_c/δ lead to large secondary motions of the time-averaged flow. These motions are reflected in the non-zero values of $\widetilde{u}$ in the outer layer. These motions develop even for case S, which does not show dominant spanwise wavelength larger than δ.

The main difference between the two rough cases is that case T is characterized by a higher dispersive stress anisotropy (with more intense $\widetilde{u}$ and weaker $\widetilde{v}$ and $\widetilde{w}$). The temporal variations of peak values of the wall-normal profiles of dispersive stress are compared in Fig. 7(a)-(c). It is shown that the rapid initial increase and subsequent decrease in peak values take place rather synchronously for both cases, except for $\langle\widetilde{v}^2\rangle$, which recovers at $t^* \approx 1$ in case T, compared to $t^* \approx 3$ in case S.

For both rough cases, $u_\tau(t)^2/U_R(t)^2$ in Fig. 5(d) and near-wall dispersive stresses in Fig. 7(a-c) approach steady-state values at almost the same time of $t^* = 3$. This may be

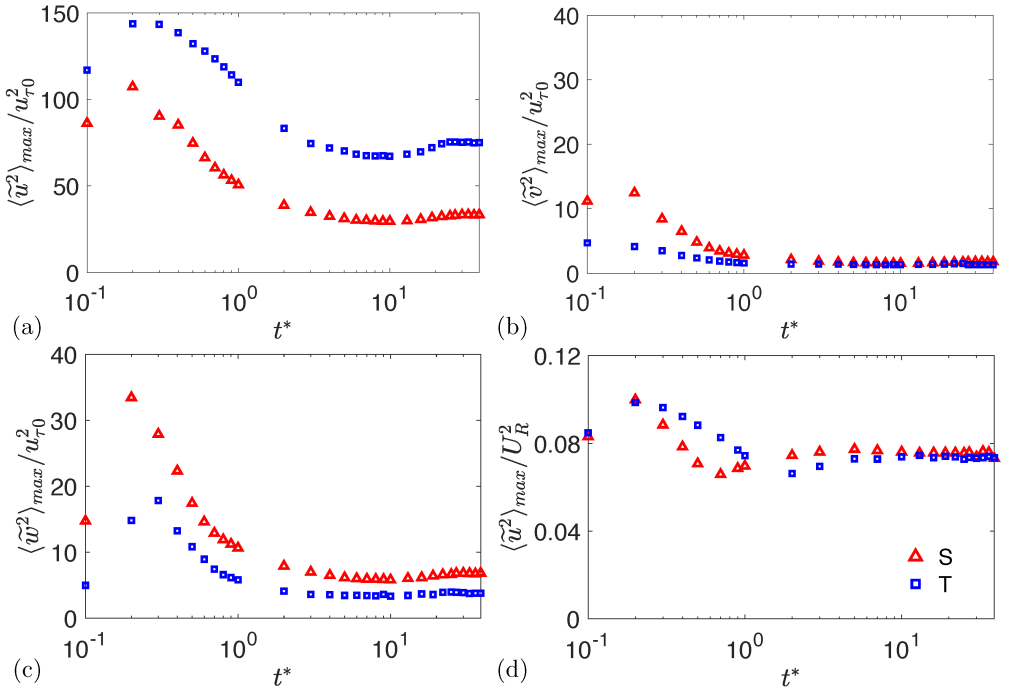

FIGURE 7. Time variation of wall-normal peak value of (a) streamwise, (b) wall-normal and (c) spanwise normal components of dispersive stress tensor, normalized by $u_{\tau 0}^2$. (d) Peak value of streamwise component normalized by instantaneous U_R^2.

explained by the dependence of u_τ^2 (or the total drag) on roughness-scale flow separations, which are associated with intense $\widetilde{u}_i$ perturbations. To demonstrate such dependence, the variation of the $\langle\widetilde{u}^2\rangle$ peak value normalized by U_R^2 is plotted in Fig. 7(d). One observes that the large variation (72% of the maximum value in time) of $\langle\widetilde{u}^2\rangle_{\max}$ scaled using $u_{\tau 0}$ in Fig. 7(a) becomes much weaker (34% of the maximum value in time) when scaled using the instantaneous U_R. The residual time variation in Fig. 7(d) is attributed to the non-equilibrium transient process, and possibly to the transition from the initial transitionally rough flow to a later fully rough flow.

Given that the $\langle\widetilde{u}_i^2\rangle(y)$ profile shape varies little throughout (Fig. 6), normalizing the profile values using U_R^2 would yield dispersive stress curves that are rather invariant in time. This suggests that most of the temporal variations of $\langle\widetilde{u}_i^2\rangle(y)$ is absorbed by $U_R(t)^2$.

In other words, the mean flow pattern $\overline{u}_i(\boldsymbol{x})/U_R$ inside the sublayer appears to stay close to equilibrium during the transient.

4.4. *Temporal variations of Reynolds stresses*

For a transient accelerating channel on a smooth wall, He & Seddighi (2013) showed that $\langle\overline{v'^2}\rangle$ and $\langle\overline{w'^2}\rangle$ are frozen in the initial stage of transient, leading to a quasi-one-dimensional turbulence. Similar observations on a smooth wall were also made by various researchers from spatially developing boundary layers under strong acceleration.

The variation of Reynolds stresses on the two rough walls are shown in Fig. 8. The Reynolds stresses are normalized with $u_{\tau 0}$, to show variations of the stress magnitude. Unlike the smooth case described by He & Seddighi (2013), on the present rough walls all

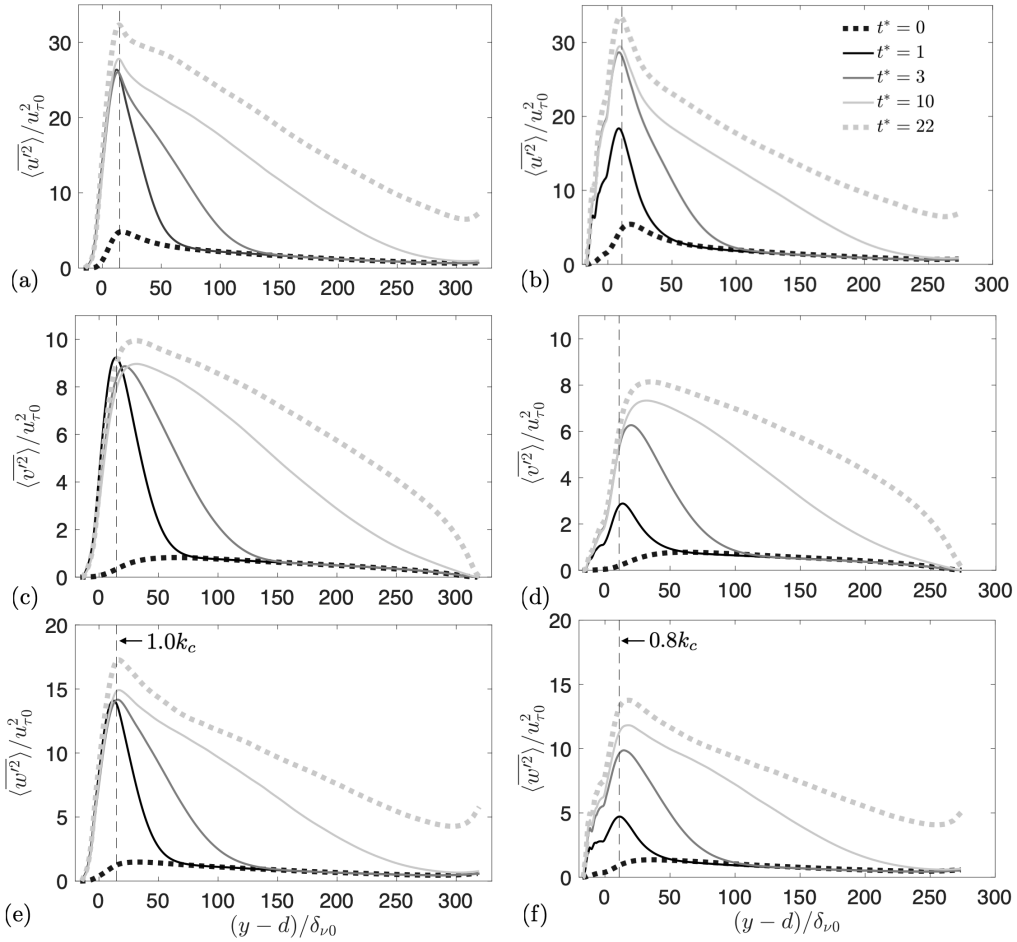

FIGURE 8. Wall-normal profiles of Reynolds stresses, at representative times for S (a,c,e) and T (b,d,f) cases.

components increase rapidly towards the new steady state, starting from the near-wall region. During the rapid augmentation of Reynolds stresses, the peak elevations of all normal components in case S appear to coincide at $1.0k_c$. This indicates that the new turbulence generation immediately after the acceleration occurs at the crest height and is closely linked to the dynamics of flow around tall roughness protuberances. Similarly, for case T, the augmented streamwise Reynolds stress peaks constantly at $0.8k_c$ for T roughness. However, for this roughness the peaks of wall-normal and spanwise Reynolds stresses move from $0.8k_c$ toward the crest height at late times, probably due to the wide variation in local roughness peak heights brought by the surface heterogeneity. Between the two rough cases, close to the wall all normal Reynolds stresses increases faster in the S case than in T. In both cases, the development of the outer layer profiles lags significantly behind that of the near-wall profiles; the equilibrium states in the outer layer are achieved at around $t^* = 22$.

Figure 9 tracks the time variation of the peak value of Reynolds stress profiles. A dependency on the roughness geometry is evident. For the smooth case, $\langle \overline{v'^2} \rangle$ and $\langle \overline{w'^2} \rangle$

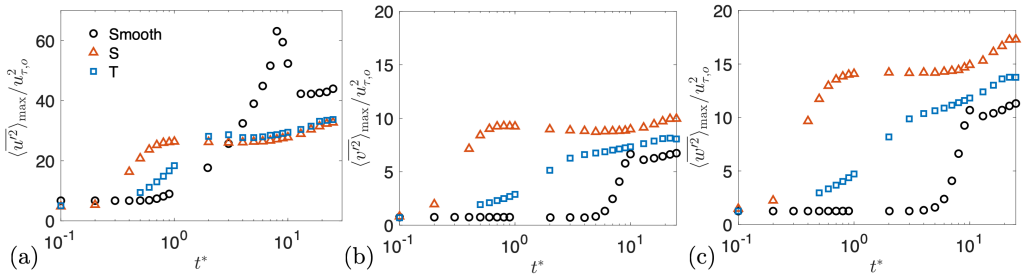

FIGURE 9. Time variation of wall-normal peak value of (a) streamwise, (b)wall-normal and (c) spanwise normal components of Reynolds stress tensor (normalized by $u_{\tau 0}^2$).

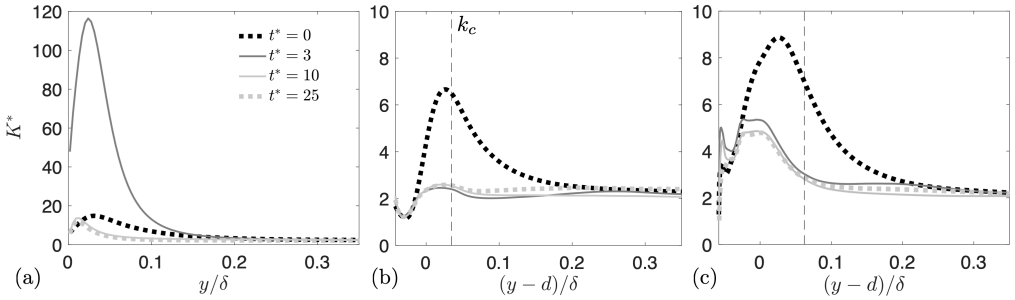

FIGURE 10. Variation of anisotropy parameter K^* at various t^* for (a) smooth-wall, (b) S and (c) T cases. --- Steady states.

peak values remain almost frozen for a significant period of time till $t^* \approx 5$ (corresponding to the stage when C_f decreases), while $\langle \overline{u'^2} \rangle$ peak increases. For $t^* > 5$, $\langle \overline{v'^2} \rangle$ and $\langle \overline{w'^2} \rangle$ rapidly increase, marking the phase of retransition. The streamwise fluctuations overshoot over the steady-state value before the new equilibrium state is reached. This is associated with both the newly generated TKE predominantly resting in u' and the retransition process. Overshoots (though weaker) are also observed for other normal Reynolds stress components. Theses observations are consistent with those described by He & Seddighi (2013). A drastic difference brought by the presence of roughness is the rapid increase of all normal Reynolds stress components starting at the beginning of the transient. All normal components increase much faster for surface S.

The combination of Figs. 8 and 9 reveals two stages of Reynolds-stress recovery from an abrupt acceleration on rough walls: (1) an initial stage of rapid recovery of Reynolds stresses inside the RSL as shown in Fig. 8, together with a rapid variation of u_τ/U_R (Fig. 5(d)) toward the steady state (till around $t^* = 1$ in case S and $t^* = 3$ in case T); and (2) a second stage ($t^* > 1$ for case S and $t^* > 3$ for T) marked mainly by the variation of the outer-layer Reynolds stresses.

Figure 10 shows the variation of anisotropy parameter (or the streamwise energy partition parameter) defined by Lee *et al.* (1990) as

$$K^*(y,t) = \frac{2\langle \overline{u'^2} \rangle}{\langle \overline{v'^2} \rangle + \langle \overline{w'^2} \rangle}. \tag{4.2}$$

As an overall measure of the Reynolds stress anisotropy, K^* quantifies the distribution of TKE among streamwise fluctuations and those in the other two directions. Profiles of

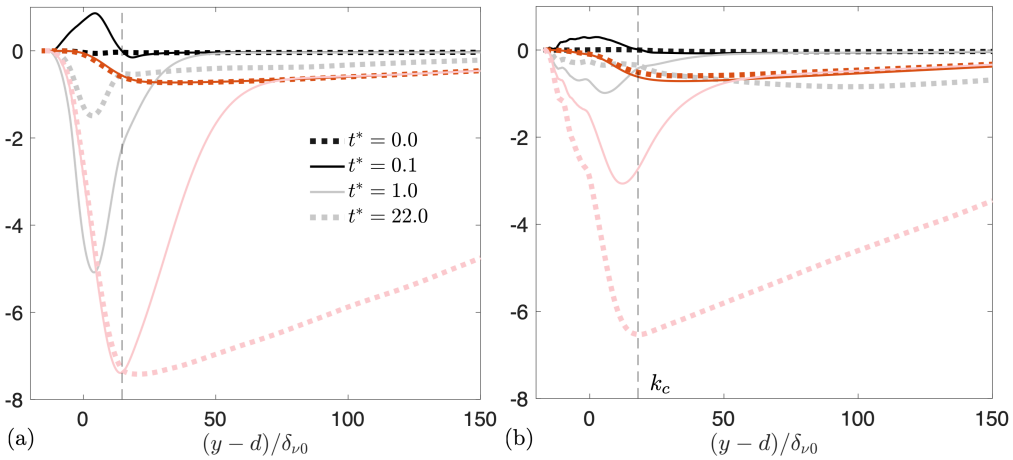

FIGURE 11. Wall-normal profiles of dispersive (black and grey) and Reynolds (red and light red) shear stresses, normalized by $u_{\tau 0}$ for cases (a) S and (b) T cases.

K^* for all cases are compared in Fig. 10 at several t^*. For the smooth case in the early stage ($t^* < 3$), K^* increases rapidly near the wall from its initial steady-state profile, indicating flow development toward quasi-one-dimensional turbulence. On the rough walls, in contrast, the Reynolds stress anisotropy monotonically decreases, recovering to the long time values well before $t^* = 3$; the subsequent slow recovery of outer-layer Reynolds stresses does not alter the anisotropy. The difference between the initial and final steady states for the rough cases is because the flows are not fully rough at $Re_{\tau 0}$. Compared to case S, case T yields higher Reynolds stress anisotropy for all t^*.

Figure 11 compares the dispersive shear and the Reynolds shear stresses. For both roughnesses, in the initial and final steady states $\langle \widetilde{u}\,\widetilde{v} \rangle$ is significantly weaker than $\langle \overline{u'v'} \rangle$. During the transient, however, $\langle \widetilde{u}\,\widetilde{v} \rangle$ becomes significant below k_c, sometimes surpassing the Reynolds shear stress. Thus, the dispersive shear stress can be dynamically important for mean-flow response in a developing flow. We note also that the dispersive shear stress becomes positive (with small magnitudes) for a brief time at the beginning of the transient. It remains an interesting question for future work as to what contributes to this phenomenon.

We now explain the earlier observations on the logarithmic slope of U profiles shown in Fig. 4, namely, the increase of κ in rough-wall cases at early t^* and the faster recovery of κ for S than for T. On a smooth wall, the increase of κ under a favorable pressure gradient was explained by Nickels (2004) as a result of departure of the velocity scale of attached eddies from the scale of u_τ, i.e.

$$\frac{\kappa}{\kappa_o} = \frac{u_\tau}{U_T}, \tag{4.3}$$

where κ_o is a universal von Kármán constant measured from canonical flows with zero pressure gradient, y_c is the critical y at which the near-wall sublayer 'becomes unstable' (van Driest & Blumer 1963), $U_T \equiv \sqrt{\tau(y_c)/\rho}$ is the critical velocity scale of the sublayer (i.e. velocity scale of the attached eddies), and $\tau(y)$ is the total shear stress. By fitting smooth-wall data with a wide range of streamwise pressure gradients, Nickels (2004) identified y_c^+ to be around 10 to 14. With the presence of rough wall herein, we take $y_c = k_c$ for simplicity; a supporting argument for this choice is that the negative peak of

combined Reynolds and dispersive shear stress is located at around k_c for both S and T for all t^* (Fig. 11). This stress is then considered to set the velocity scale of the attached eddies. After the impulse acceleration, u_τ is higher than its steady-state value (Fig. 4(a)), while $\tau(k_c) \approx \rho\langle\overline{u'v'}\rangle(k_c) + \rho\langle\widetilde{u}\,\widetilde{v}\rangle(k_c)$ is lower than its steady state value. Since in the steady state, $\tau(k_c) \approx u_\tau^2$ (Yuan & Piomelli 2015), this means $\kappa/\kappa_o > 1$ according to Eq. (4.3). In addition, the faster recovery of κ on S roughness is due to the fast recovery of its $\tau(k_c)$ to the steady state value—as early as $t^* \approx 1.0$ (Fig. 11(a)); at this point Eq. (4.3) yields $\kappa/\kappa_o \approx 1$.

Results in this section show that turbulence inside the RSL develops rapidly to the new steady state, while the outer layer varies slowly. The role of roughness geometry comes in by affecting the rate of response of turbulence inside the RSL and, in doing so, affecting the rate of recovery farther from the wall.

4.5. *Temporal variations of Reynolds stress budget balances*

The budget equation of the normal Reynolds stresses $\langle\overline{u'_\alpha u'_\alpha}\rangle_s$ (no summation on Greek indices) in a transient half-height channel flow on a rough wall is extended from the equation for a fully-developed open-channel flow on a rough wall (Mignot *et al.* 2009) and reads

$$\frac{\partial\langle\overline{u'^2_\alpha}\rangle_s}{\partial t} = \underbrace{\left[\underbrace{-2\langle\overline{u'_\alpha v'}\rangle_s\frac{\partial\langle\overline{u}_\alpha\rangle}{\partial y}}_{P_s} + \underbrace{P_w + P_m}_{P_s^f}\right]}\underbrace{-\left\langle\frac{\partial}{\partial x_j}\widetilde{u'_\alpha u'_\alpha}\widetilde{u}_j\right\rangle_s}_{T_w} \underbrace{-\left\langle\frac{\partial}{\partial x_j}\overline{u'_\alpha u'_\alpha u'_j}\right\rangle_s}_{T_t}$$
$$\underbrace{-2\left\langle\overline{P'\frac{\partial u'_\alpha}{\partial x_\alpha}}\right\rangle_s}_{\Pi} \underbrace{-2\frac{\partial\langle\overline{P'u'_\alpha}\rangle_s}{\partial x_\alpha}}_{T_p} \underbrace{+\nu\left\langle\frac{\partial^2\overline{u'^2_\alpha}}{\partial x_j\partial x_j}\right\rangle_s}_{T_\nu} \underbrace{-2\nu\left\langle\overline{\frac{\partial u'_\alpha}{\partial x_j}\frac{\partial u'_\alpha}{\partial x_j}}\right\rangle_s}_{\epsilon}, \quad (4.4)$$

where the terms on the right-hand-side are, respectively, shear production due to shear of DA velocity (P_s), additional shear production due to shear of the form-induced velocities (P_s^f, as the sum of the wake production $P_w = -2\langle\widetilde{u'_\alpha u'_j}\partial\widetilde{u}_\alpha/\partial x_j\rangle_s$ (Raupach & Shaw 1982) and a correction term $P_m = -2\langle\overline{u'_\alpha u'_j}\rangle\langle\partial\widetilde{u}_\alpha/\partial x_j\rangle_s$ (Mignot *et al.* 2009)), transport due to form-induced velocities (T_w), turbulent transport (T_t), viscous transport (T_ν), pressure strain rate (Π), pressure transport (T_p), and viscous dissipation (ϵ). The interface cells are not included in performing the spatial averaging in the present IBM framework. If the interface cells are also included, an additional term $2\langle\overline{F'_\alpha u'_\alpha}\rangle_s$—with a small magnitude of 4% of P_s peak value appears due to the IBM body force, but the nature of the balance is not affected. This point was discussed by Yuan & Aghaei Jouybari (2018). For the smooth case, Eq. (4.4) still applies with the form-induced terms P_s^f and T_w equal to zero. For all cases the residuals of Eq. (4.4) obtained in the steady states are up to 1% of the peak value of P_s. Here, the budget balance refers to the left-hand-side and right-hand-side of Eq. (4.4) being equal. The balance applies to all t^*.

The budget terms in the smooth case are discussed first. Figure 12 shows the sources terms of u' energy ($P_{s,11}$) and of v' energy (pressure work, $\Pi_{22} + T_{p22}$) at several time instances: (1) the initial state, (2) $t^* = 3$ (quasi-laminarization stage) and (3) $t^* = 5$ (near the onset of retransition). Figure 12(a) shows that $P_{s,11}$ increases steadily throughout the quasi-laminarization stage, leading to intensification of u' (i.e. $\partial\langle\overline{u'^2}\rangle_s/\partial t > 0$) immediately after $t^* = 0$. In comparison, the pressure work remains almost frozen in the quasi-laminarization stage. Consequently, the v' intensity remains around the initial

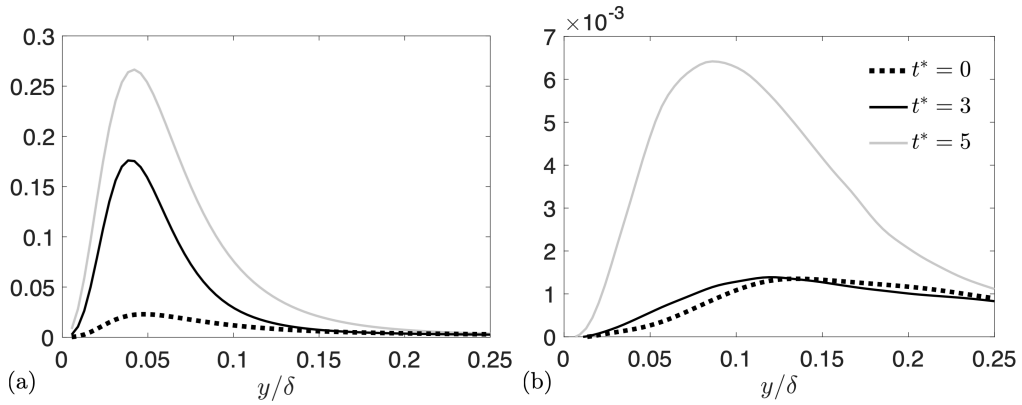

FIGURE 12. Reynolds stress budget terms in the smooth-wall case, normalized by u_{b0} and δ. (a) Shear production for $\langle\overline{u'^2}\rangle_s$ and (b) pressure work for $\langle\overline{v'^2}\rangle_s$.

level in this stage, as shown at $t^* = 3$ in Fig. 9. A similar slow response of pressure work for w' energy is also observed (not shown). The delay in increase of v' and w' intensities together with the immediate augmentation of u' leads to the much increased Reynolds stress anisotropy and quasi-one-dimensional turbulence during quasi-laminarization.

In the presence of roughness, a different balance from that in the smooth case is observed immediately after $t^* = 0$. Figure 13 shows the budget for u' and v' energy for case S, at four characteristics time instances: $t^* = 0$, $t^* = 0.1$ and 0.5 (two instances in the stage of rapid development of RSL turbulence), and $t^* = 1$ (after the RSL is fully developed). Comparison with the balances at $t^* = 25$ (not shown) suggests that the near-wall balance recovers to the steady state at $t^* \approx 1.0$. For the streamwise Reynolds stress, P_s^f takes positive values with significant magnitudes in both the transient and the final steady state, though the magnitudes are smaller compared to the magnitudes of P_s and Π in most of the RSL. The time-rate-of-change term remains positive (indicating augmentation of u') till $t^* \approx 1.0$. For the wall-normal Reynolds stress, P_s^f also takes significant magnitudes. At $t^* = 0.1$, P_s^f is of similar magnitude as Π. At this time, the time-rate-of-change of $\langle\overline{v'^2}\rangle$ is positive and peaks roughly at the elevation of the P_s^f peak. At later times (shown at $t^* = 0.5$ as an example), the Π magnitude overtakes that of P_s^f. The steady state is recovered at $t^* = 1$ for the near-wall balance of v' energy also. The subsequent recovery of outer-layer budget terms does not modify the nature of the balance.

The same budget terms are shown in Fig. 14 for case T, also at four characteristic time instances. The first three of the four t^* instances are chosen to be the same as in Fig. 13, while the last time is chosen at a slightly later time of $t^* = 3$, at which RSL becomes fully developed for case T. For the streamwise Reynolds stress, P_s^f shows a rather complex pattern, as its sign changes for different y and t^*. Recall that P_s^f represents the amount of kinetic energy transferred from $\widetilde{u}_i$ kinetic energy (or 'wake kinetic energy', WKE, termed by Raupach & Shaw (1982)) at scales larger than turbulent eddies to the TKE by shear production. Such complex dependence of the sign of P_s^f on the wall-normal distance and time may suggest a competition between TKE-to-WKE and WKE-to-TKE transfers. On a multiscale roughness, it is possible that both very large u' scales and very small $\widetilde{u}_i$ scales exist, contributing to local energy transfer from TKE to WKE. For the wall-normal Reynolds stress, case T also yields large magnitudes of P_s^f in the initial stage

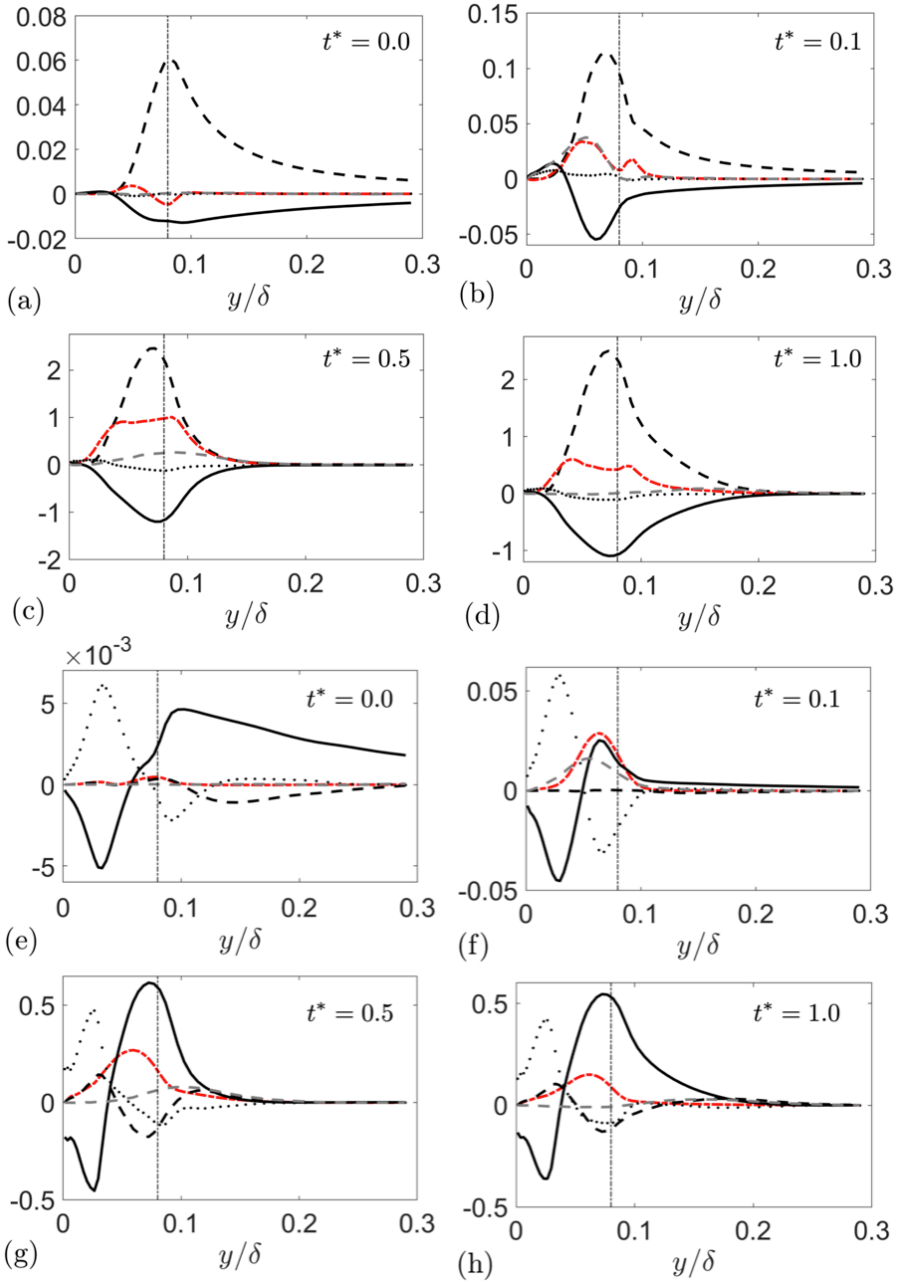

FIGURE 13. Budget balance for $\langle\overline{u'^2}\rangle_s$ (a-d) and $\langle\overline{v'^2}\rangle_s$ (e-h) in case S. Budget terms are normalized by u_{b0} and δ. Vertical line indicates $y/k_c = 1$. - - - $\partial/\partial t$ term; - · - P_s^f; ——— Π; In (a-d), - - - P_s; in (e-f), - - - T_t, ··· T_p.

of RSL development, although $P_s^f \ll \Pi$ in the steady states. In both cases, P_s^f remains positive for all t^* and all elevations for the $\langle\overline{v'^2}\rangle$ budget, indicating energy transfer from $\widetilde{v}$ to v' motions. This is probably because intense v' values (associated with small-scale active motions) occur typically at a scale smaller than the characteristic lengthscale of

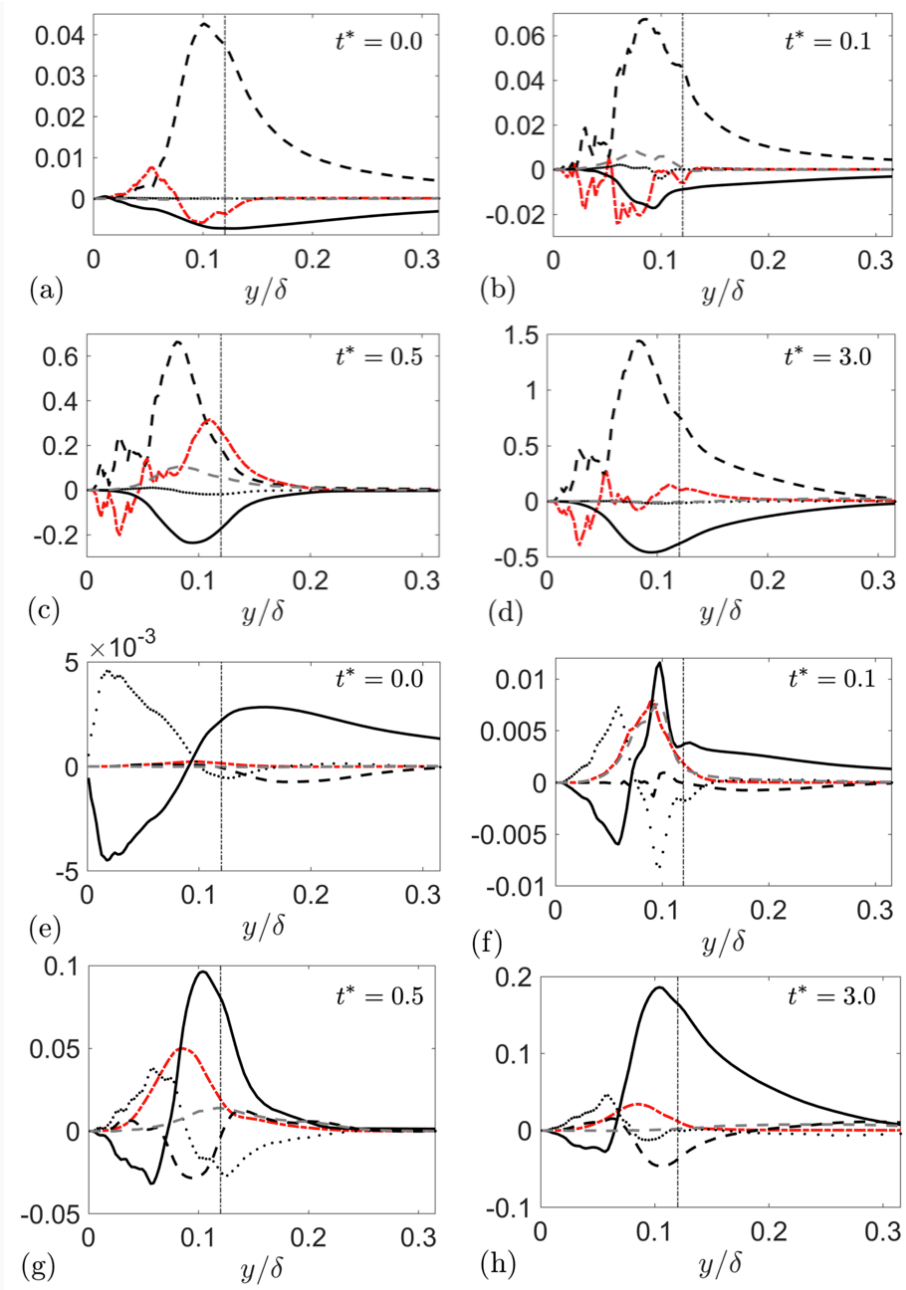

FIGURE 14. Budget balance for $\langle\overline{u'^2}\rangle_s$ (a-d) and $\langle\overline{v'^2}\rangle_s$ (e-h) in case T. Budget terms are normalized by u_{b0} and δ. Vertical line indicates $y/k_c = 1$. - - - $\partial/\partial t$ term; - - P_s^f; —— Π; In (a-d), - - - P_s; in (e-f), - - - T_t, - - T_p.

the time-mean velocity variation.

In summary, the similarities between the two rough cases include: (1) the immediate augmentation of P_s^f, especially important for $\langle\overline{v'^2}\rangle$ production; (2) the subsequent increase of Π, which later becomes the dominant source of $\langle\overline{v'^2}\rangle$ as P_s^f weakens in time;

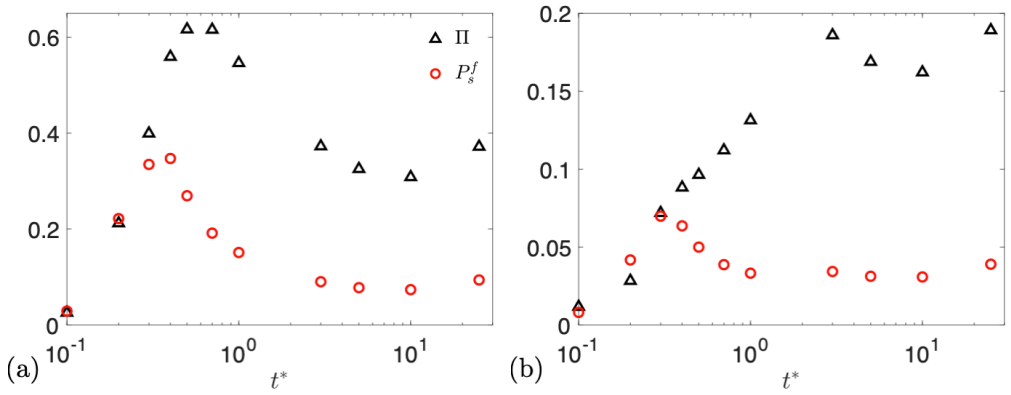

FIGURE 15. Temporal evolution of the positive peak values of Π and the peak values of P_s^f (both normalized by u_{b0} and δ) in $\langle\overline{v'^2}\rangle$ budget in cases S (a) and T (b).

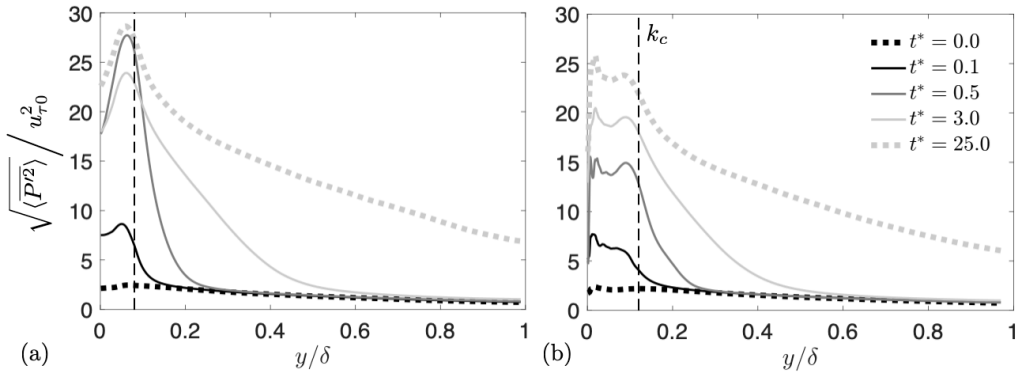

FIGURE 16. Wall-normal profiles of P' rms (normalized by $u_{\tau 0}^2$) for cases (a) S and (b) T at different t^*.

and that (3) the $\langle\overline{u'^2}\rangle$ budget balance is also modified by P_s^f, which takes significant magnitudes during the transient.

The main effect of the roughness geometry appears to be reflected in different rates of recovery of the budget balance. Here, we focus on the $\langle\overline{v'^2}\rangle$ budget, as the temporal variation of its balance is more significant than that for $\langle\overline{u'^2}\rangle$. Figure 15 compares the temporal variation of the peak values of Π and P_s^f for cases S and T. The sign of Π changes inside the RSL; the positive peak of Π is shown here to better represent the nature of this term being an overall source for $\langle\overline{v'^2}\rangle$. It is shown that for both surfaces P_s^f peaks at a similar t^* of around 0.3-0.4. This is because that P_s^f depends on $\partial\widetilde{u}_i/\partial x_j$, and that the time variations of the dispersive stresses between cases S and T are almost synchronous due to the approximate scaling of $\widetilde{u}_i$ on U_R. In contrast, Π increases and peaks at $t^* \approx 0.5$-0.7 for case S, while it peaks much later—at $t^* \approx 3$—for case T. To provide further explanation to the different timing of Π term recovery, Fig. 16 compares the time variation of the pressure fluctuation RMS profiles between S and T cases; a faster recovery of near-wall P' intensity is seen for case S. Specifically, the P' RMS values below k_c in case S almost reach their steady state values at $t^* = 0.5$, while in case T they continue to increase in large time.

To provide insights as to why the P' intensity varies differently between cases S and

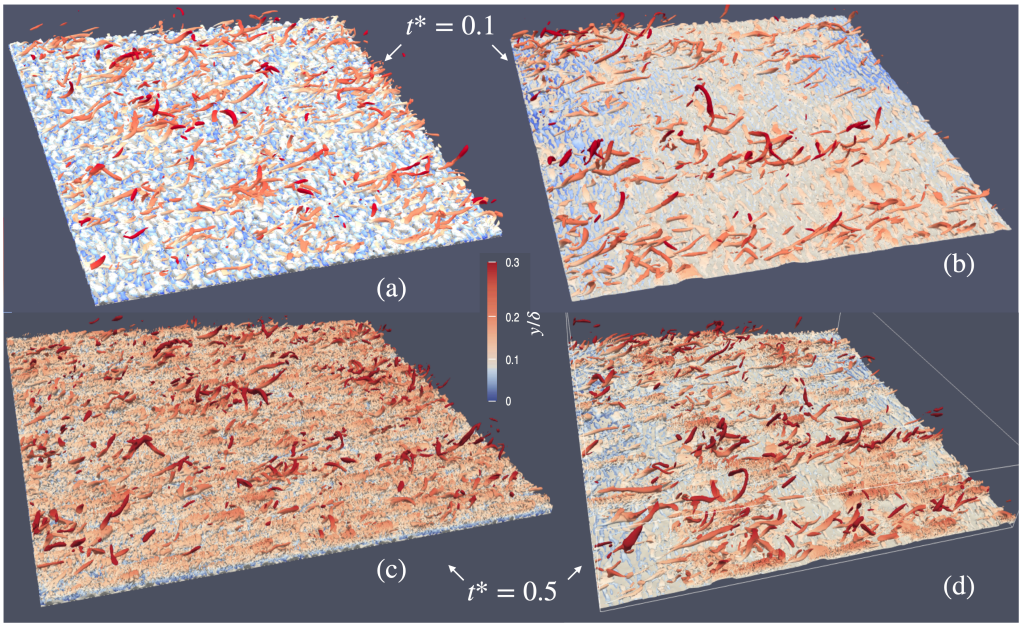

FIGURE 17. Q-isosurfaces at (a-b) $t^* = 0.1$ and (c-d) $t^* = 0.5$ for (a,c) case S and (b,d) case T colored by distance to wall and rough surface colored in white.

T, Fig. 17 compares the coherent vortical turbulent motions visualized using the second-invariant of the velocity gradient tensor,

$$Q = -\frac{1}{2}\frac{\partial u_i}{\partial x_j}\frac{\partial u_j}{\partial x_i}. \tag{4.5}$$

The generation of new turbulence of small scales during $0.1 < t^* < 0.5$ are evident. These motions are located at y of 0.1-0.2δ (in the vicinity of k_c). On surface S, these newly generated eddies are widespread in the horizontal plane, as the roughness protuberances are closely packed. On surface T, in comparison, the distribution of these motions are more spotty, associated with more sparsely distributed high-slope roughness peaks. It is conjectured that the large wavelengths (with mild slopes) of surface T does not lead to flow separation or strong $\partial\widetilde{u}_i/\partial x_j$ that generates v' energy through P_s^f, while the sparsely distributed small-wavelength peaks produce turbulence, which then slowly spread to cover the whole horizontal domain. As the P' distribution is related to vortical motions, the P' RMS develops more gradually in case T.

5. Conclusions

Direct numerical simulations of the impulse response of half-height channel flows on a smooth wall and two rough surfaces to a step increase of bulk velocity are carried out. Two roughness geometries are included: a densely distributed sandgrain roughness (case S) and a multiscale turbine-blade roughness (case T). Both cases share the same mean roughness height and develop from a transitionally rough flow to a fully rough one during the transient. Different flow responses between the rough and smooth cases, as well as between the two rough cases, are discussed. As seen in the existing literature of temporally and spatially accelerated flows, turbulence over a smooth wall undergoes a

quasi-laminarization process, characterized by high Reynolds stress anisotropy caused by a delayed response of the TKE redistribution to the acceleration. These phenomena are not observed in the presence of roughness.

On rough walls, the roughness sublayer layer (RSL) thickness stays almost constant during the transient. Inside the RSL, the temporal variations of the form-induced fluctuation are largely absorbed when normalized by the instantaneous mean velocity at the edge of the RSL (i.e., U_R). This indicates that the ensemble-averaged flow ($\overline{u}/U_R$) in the sublayer stays close to equilibrium during the transient.

Two stages of the turbulence recovery from an abrupt acceleration on a rough wall toward the new steady state are observed, including: (1) a short, initial stage of rapid recovery of hydrodynamic drag and increase of RSL turbulent intensities till their early recovery to the long-time values, and (2) a slower second stage marked mainly by the variations of the outer-layer Reynolds stresses. In the second stage, the Reynolds stress balance is similar to the steady state, while during the first stage a fundamental change of Reynolds stress balance is observed. In particular, the magnitude of the form-induced production P_s^f becomes much larger than in the steady state, strikingly so for $\langle\overline{v'^2}\rangle$. The result is a rapid augmentation of TKE and a decrease of Reynolds stress anisotropy, manifested by the generation of small-scale new turbulence in regions of intense form-induced shear. Also, in the first stage the total shear stress at roughness crest is significantly lower than the wall shear stress, leading to a reduced logarithmic slope of the mean velocity. The roughness geometry affects the rate of recovery of the RSL turbulence. A slower recovery of TKE redistribution (due to a slower amplification of pressure fluctuations) is seen in case T. This is associated with sparsely distributed small-wavelength roughness peaks, producing new turbulence which takes time to spread and cover the whole domain.

This work provides detailed explanations on how roughness suppresses reverse transition in a non-equilibrium accelerated turbulence. Results indicate that, unlike fully-developed wall bounded turbulence where outer-layer similarity applies and the roughness sublayer flow affects the value of u_τ only, in the present non-equilibrium transient flows the sublayer details play a more important role by determining the rate of flow recovery throughout the boundary layer. Future work is needed to extend this work to spatially developing turbulent boundary layers.

Acknowledgements

The authors gratefully acknowledge the financial support of the Office of Naval Research (Award No. N00014-17-1-2102). Computational support was provided by Michigan State University's Institute for Cyber-Enabled Research.

REFERENCES

Barros, J. M., Schultz, M. P. & Flack, K. A. 2018 Measurements of skin-friction of systematically generated surface roughness. *Int. J. Heat Fluid Flow* **72**, 1–7.

Bourassa, C. & Thomas, F. O. 2009 An experimental investigation of a highly accelerated turbulent boundary layer. *J. Fluid Mech.* **634**, 359–404.

Cal, R. B., Brzek, B., Johansson, T. & Castillo, L. 2009 The rough favourable pressure gradient turbulent boundary layer. *J. Fluid Mech.* **641**, 129–155.

Cheng, W., Pullin, D. I. & Samtaney, R. 2015 Large-eddy simulation of separation

and reattachment of a flat plate turbulent boundary layer. *J. Fluid Mech.* **785**, 78–108.

Chung, D., Hutchins, N., Schultz, M. P. & Flack, K. A. 2021 Predicting the drag of rough surfaces. *Annu. Rev. Fluid Mech.* **53**, 439–471.

van Driest, E. R. & Blumer, C. B. 1963 Boundary layer transition-freestream turbulence and pressure gradient effects. *AIAA J.* **1**, 1303–1306.

Ghodke, C. D. & Apte, S. V. 2016 DNS study of particle-bed–turbulence interactions in an oscillatory wall-bounded flow. *J. Fluid Mech.* **792**, 232–251.

Ghodke, C. D. & Apte, S. V. 2017 A numerical investigation to study roughness effects in oscillatory flows. In *Proceedings of the ASME 2017 Fluids Engineering Division Summer Meeting*.

He, S. & Jackson, J. D. 2000 A study of turbulence under conditions of transient flow in a pipe. *J. Fluid Mech.* **408**, 1–38.

He, S. & Seddighi, M. 2013 Turbulence in transient channel flow. *J. Fluid Mech.* **715**, 60–102.

He, S. & Seddighi, M. 2015 Transition of transient channel flow after a change in Reynolds number. *J. Fluid Mech.* **764**, 395–427.

Jackson, P. S. 1981 On the displacement height in the logarithmic velocity profile. *J. Fluid Mech.* **111**, 15–25.

Jiménez, J. 2004 Turbulent flows over rough walls. *Annu. Rev. Fluid Mech.* **36**, 173–196.

Jones, W. P. & Launder, B. E. 1972 The prediction of laminarization with a two-equation model of turbulence. *Int. J. Heat Mass Transfer* **15**, 301–314.

Keating, A., Piomelli, U., Bremhorst, K. & Nešić, S. 2004 Large-eddy simulation of heat transfer downstream of a backward-facing step. *J. Turbul.* **5**, N20.

Lee, M. J., Kim, J. & Moin, P. 1990 Structure of turbulence at high shear rate. *J. Fluid Mech.* **216**, 561–583.

Mejia-Alvarez, R. & Christensen, K. T. 2013 Wall-parallel stereo particle-image velocimetry measurements in the roughness sublayer of turbulent flow overlying highly irregular roughness. *Phys. Fluids* **25**, 115109–1–24.

Mignot, E., Bartheleemy, E. & Hurther, D. 2009 Double-averaging analysis and local flow characterization of near-bed turbulence in gravel-bed channel flows. *J. Fluid Mech.* **618**, 279–303.

Moser, R. D. & Moin, P. 1987 The effects of curvature in wall-bounded turbulent flows. *J. Fluid Mech.* **175**, 479–510.

Na, Y. & Moin, P. 1998 The structure of wall-pressure fluctuations in turbulent boundary layers with adverse pressure gradient and separation. *J. Fluid Mech.* **377**, 347–373.

Nagib, H. M. & Chauhan, K. A. 2008 Variations of von Kármán coefficient in canonical flows. *Phys. Fluids* **20**, 15180–1–10.

Narasimha, R. & Sreenivasan, K. R. 1973 Relaminarization in highly accelerated turbulent boundary layers. *J. Fluid Mech.* **61**, 417–447.

Nickels, T. B. 2004 Inner scaling for wall-bounded flows subject to large pressure gradients. *J. Fluid Mech.* **521**, 217–239.

Nikora, V., Koll, K., McEwan, I., McLean, S. & Dittrich, A. 2004 Velocity distribution in the roughness layer of rough-bed flows. *J. Hydr. Engng* **130**, 1036–1042.

Passalacqua, P., Porté-Agel, F., Foufoula-Georgiou, E. & Paola, C. 2006

Application of dynamic subgrid-scale concepts from large-eddy simulation to modeling landscape evolution. *Water Resour. Res.* **42**, W06D11–1–11.

Piomelli, U. & Yuan, J. 2013 Numerical simulations of spatially developing, accelerating boundary layers. *Phys. Fluids* **25**, 101304–1—21.

Pokrajac, D., Campbell, L. J., Nikora, V. & Manes, C. adn McEwan, I. 2007 Quadrant analysis of persistent spatial velocity perturbations over square-bar roughness. *Exp. Fluids* **42**, 413–423.

Pope, S. B. 2000 *Turbulent Flows*. Cambridge, U.K.: Cambridge Univ. Press.

Raupach, M. R., Antonia, R. A. & Rajagopalan, S. 1991 Rough-wall boundary layers. *Appl. Mech. Rev.* **44**, 1–25.

Raupach, M. R. & Shaw, R. H. 1982 Averaging procedures for flow within vegetation canopies. *Bound.-Lay. Meteorol.* **22**, 79–90.

Scotti, A. 2006 Direct numerical simulation of turbulent channel flows with boundary roughened with virtual sandpaper. *Phys. Fluids* **18**, 031701–1—4.

Seddighi, M., He, S., Pokrajac, D., O'Donoghue, T. & Vardy, A. E. 2015 Turbulence in a transient channel flow with a wall of pyramid roughness. *J. Fluid Mech.* **781**, 226–260.

Skote, M. & Henningson, D. S. 2002 Direct numerical simulation of a separated turbulent boundary layer. *J. Fluid Mech.* **471**, 107–136.

Tachie, M. F., Agelin-Chaab, M. & Shah, M. K. 2007 Turbulent flow over transverse ribs in open channel with converging side walls. *Int. J. Heat Fluid Flow* **28**, 683–707.

Vanderwel, C. & Ganapathisubramani, B. 2015 Effects of spanwise spacing on large-scale secondary flows in rough-wall turbulent boundary layers. *J. Fluid Mech.* **774**, R2.

Volino, R. J. 2020 Non-equilibrium development in turbulent boundary layers with changing pressure gradients. *J. Fluid Mech.* **897**, A2–1–48.

Wu, W. & Piomelli, U. 2018 Effects of surface roughness on a separating turbulent boundary layer. *J. Fluid Mech.* **841**, 552–580.

Yang, J. & Anderson, W. 2018 Numerical study of turbulent channel flow over surfaces with variable spanwise heterogeneities: Topographically-driven secondary flows affect outer-layer similarity of turbulent length scales. *Flow, Turb. Combust.* **100**, 1–17.

Yuan, J. & Aghaei Jouybari, M. 2018 Topographical effects of roughness on turbulence statistics in roughness sublayer. *Phys. Rev. Fluids* **3**, 114603.

Yuan, J. & Brereton, G. J. 2019 Effect of fractal-like surface roughness on fully developed channel flow. In *Proceedings of TSFP-11*.

Yuan, J. & Piomelli, U. 2014*a* Estimation and prediction of the roughness function on realistic surfaces. *J. Turbul.* **15**, 350–365.

Yuan, J. & Piomelli, U. 2014*b* Numerical simulations of sink-flow boundary layers over rough surfaces. *Phys. Fluids* **26**, 015113–1—015113–28.

Yuan, J. & Piomelli, U. 2014*c* Roughness effects on the Reynolds stress budgets in near-wall turbulence. *J. Fluid Mech.* **760**, R1.

Yuan, J. & Piomelli, U. 2015 Numerical simulation of a spatially developing accelerating boundary layer over roughness. *J. Fluid Mech.* **780**, 192–214.